

## UHI Research Database pdf download summary

### On the Sediment Dynamics in a Tidally Energetic Channel

McIlvenny, Jason; Tamsett, Duncan; Gillibrand, Philip; Goddijn-Murphy, Lonneke

*Published in:*

Journal of Marine Science and Engineering

*Publication date:*

2016

*The re-use license for this item is:*

CC BY

*The Document Version you have downloaded here is:*

Peer reviewed version

*The final published version is available direct from the publisher website at:*  
[10.3390/jmse4020031](https://doi.org/10.3390/jmse4020031)

### [Link to author version on UHI Research Database](#)

*Citation for published version (APA):*

McIlvenny, J., Tamsett, D., Gillibrand, P., & Goddijn-Murphy, L. (2016). On the Sediment Dynamics in a Tidally Energetic Channel: The Inner Sound, Northern Scotland. *Journal of Marine Science and Engineering*, 4(2).  
<https://doi.org/10.3390/jmse4020031>

#### General rights

Copyright and moral rights for the publications made accessible in the UHI Research Database are retained by the authors and/or other copyright owners and it is a condition of accessing publications that users recognise and abide by the legal requirements associated with these rights:

- 1) Users may download and print one copy of any publication from the UHI Research Database for the purpose of private study or research.
- 2) You may not further distribute the material or use it for any profit-making activity or commercial gain
- 3) You may freely distribute the URL identifying the publication in the UHI Research Database

#### Take down policy

If you believe that this document breaches copyright please contact us at [RO@uhi.ac.uk](mailto:RO@uhi.ac.uk) providing details; we will remove access to the work immediately and investigate your claim.

8 *Article*

9 **On the Sediment Dynamics in a Tidally Energetic Channel: The**  
10 **Inner Sound, Northern Scotland.**

11 Jason McIlvenny<sup>1,\*</sup>, Duncan Tamsett<sup>1,2</sup>, Philip Gillibrand<sup>1</sup> and Lonneke Goddijn-Murphy<sup>1</sup>.

12 <sup>1</sup> Centre for Energy and the Environment, Environmental Research Institute, North Highland College UHI,  
13 Ormlie Road, Thurso, KW14 7EE, U.K. E-mails: [philip.gillibrand@uhi.ac.uk](mailto:philip.gillibrand@uhi.ac.uk); [duncan.tamsett@uhi.ac.uk](mailto:duncan.tamsett@uhi.ac.uk);  
14 [lonneke.goddijn-murphy@uhi.ac.uk](mailto:lonneke.goddijn-murphy@uhi.ac.uk)

15 <sup>2</sup> Kongsberg Maritime, Underwater Mapping, Shuttleworth Close, Great Yarmouth, Norfolk, NR31 0NQ,  
16 U.K. E-mail: [duncan.tamsett@km.kongsberg.com](mailto:duncan.tamsett@km.kongsberg.com)

17 \* Author to whom correspondence should be addressed; E-mail: [jason.mcilvenny@uhi.ac.uk](mailto:jason.mcilvenny@uhi.ac.uk); Tel.: +44  
18 (0)1847 889663

19 Academic Editor:

20 *Received: / Accepted: / Published:*

21  
22 **Abstract:** Sediment banks within a fast-flowing tidal channel, the Inner Sound in the  
23 Pentland Firth, are mapped using multi-frequency side-scan sonar. This novel technique  
24 provides a new tool for seabed sediment and benthic habitat mapping. The sonar data are  
25 supplemented by sediment grab and ROV videos. The combined data provide detailed  
26 maps of persistent sand and shell banks present in the Sound despite the high energy  
27 environment. Acoustic Doppler Current Profiler data and numerical model predictions are  
28 used to understand the hydrodynamics of the system. By combining the hydrodynamics  
29 and sediment distribution data, we explain the sediment dynamics in the area. Sediment  
30 particle shape and density, coupled with persistent features of the hydrodynamics, are the  
31 key factors in the distribution of sediment within the channel. Implications for tidal energy  
32 development planned for the Sound are discussed.

33 **Keywords:** Sediment transport, hydrodynamics, settling rates, tidal energy, Pentland Firth.  
34

---

## 35 1. Introduction

36

37

38

39

40

41

42

43

44

45

46

47

48

49

50

51

52

53

54

55

56

57

58

59

60

61

62

63

64

65

66

Over the past decade, the strong tidal flows of the Pentland Firth have been a focus of attention for tidal energy developers, with a number of sites identified and leases granted for tidal energy extraction using tidal turbines. Tidal energy potential for the whole Firth has been estimated to be in the range of 1 – 18 GW [1], though Adcock et al. [2], suggest that a more realistic figure for the maximum available power is 1.9 GW. At the time of writing, the Meygen tidal turbine array, planned for the Inner Sound channel in the Firth (Figure 1), is likely to be the first commercial tidal energy array to be installed anywhere in the world. Tidal current speeds in the Inner Sound have been recorded up to 6 m s<sup>-1</sup> during flood spring tides, offering an energy resource of up to 398 MW to the Meygen project [3]. Government consent to deploy tidal turbines and marine energy generation devices in general, is generally subject to environmental impact assessment, demonstrating little or acceptable environmental effect. These assessments typically focus on collision risk for marine mammals and seabirds, which present the highest impact risks. However, other, more subtle, environmental impacts arising from the deployment of large numbers of tidal turbines can be envisaged. These have been outlined by a number of authors, with the focus being mainly on ecological and socio-economic impacts (e.g. [4], [5]).

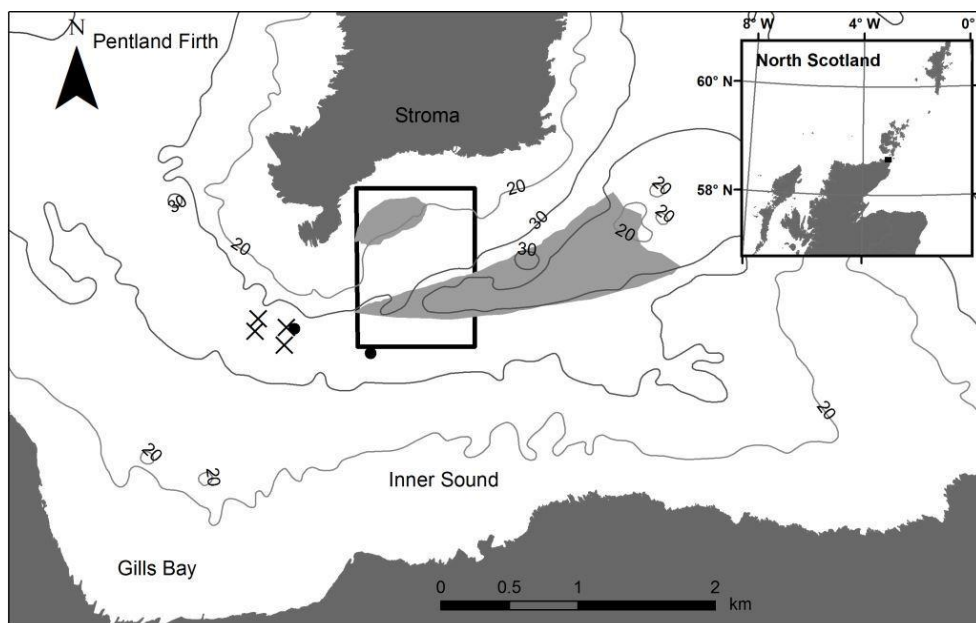


**Figure 1.** Study site location. The Inner Sound lies between the island of Stroma and Gills Bay on the Scottish mainland. The Pentland Firth lies between the mainland and the Orkney Islands. Also shown; nearshore bathymetry (contours) and the locations of the sediment banks obtained from multi-beam data [3], and ADCP data (●) referred to in Tables 2 and 3 (ADCP 1 is furthest west and ADCP 2 to the east). The positions of the first tidal turbines are noted (x).

67 To date, one of the potential impacts of tidal energy that has received less attention is sediment  
68 transport and the effect of energy extraction on the movement of sediment through these tidally  
69 energetic channels. An early study by Neill et al. [6], demonstrated that installations of tidal energy  
70 convertors in the Bristol Channel had the potential to influence large scale sediment dynamics and bed  
71 level changes, and that these impacts were most pronounced in regions where tidal asymmetry was  
72 stronger. In a further study, Neill et al. [7], found that tidal turbines could also impact sand bank  
73 formation and evolution near headlands. In the Pentland Firth, Martin-Short et al. [8], used a high  
74 resolution hydrodynamic model to identify areas of sediment erosion and deposition, based on critical  
75 bed shear stress distributions calculated by the model. They found that installing arrays of more than  
76 85 tidal turbines in the Inner Sound had the potential to significantly displace areas of sediment  
77 accumulation from the sides towards the centre of the channel, as the flow was diverted around the  
78 array. With still larger arrays of more than 240 turbines, beds of larger sized sediments, such as fine  
79 gravel and coarse sand, were also predicted to migrate towards the channel centre. A further study, by  
80 Fairley et al. [9], extended the modelled sediment transport in the Pentland Firth into predictions of  
81 bed level changes, and again investigated the possible effects of turbines deployed in the Inner Sound  
82 on sediment deposition and erosion. Changes to sediment deposition and erosion patterns are likely to  
83 have knock-on effects on benthic communities that rely on suspended organic material. Harendza [10]  
84 found that bed shear stress was closely associated to the composition and distribution of benthic  
85 assemblages in the Inner Sound, and developed site-specific habitat suitability models based on  
86 physical characteristics both in the absence and presence of tidal turbines.

87 Martin-Short et al. [8], and Fairley et al. [9], both noted that accurate sediment modelling is  
88 inhibited by a lack of detailed knowledge of local sediment deposits and transport in the area. Fairley  
89 et al. combined a variety of data to construct a map of sediment type through the Pentland Firth and  
90 surrounding area, but detail in the Inner Sound was limited. Sediment banks are known to lie to the  
91 west and south of the island of Stroma and in the surrounding region some of which are composed of  
92 carbonate shell ([11], [12], [13], [14]), but the local sediment dynamics, and the potential impacts of  
93 tidal energy extraction on the deposits, remains uncertain.

94 Understanding of the tidal flow through the Pentland Firth has advanced in recent years, due in  
95 part to the proliferation of hydrodynamic models (e.g. [1], [2], [8], [9], [15] etc.) and observational  
96 studies (e.g. [16]). Many of the numerical models utilised used unstructured grids, which allow spatial  
97 resolution in the model to be concentrated in the area of interest while allowing open boundaries to  
98 located far away. The strong flows through the Firth are generated from the hydraulic pressure head  
99 that forms across the channel due to the restriction on the propagation of the tide [15], and in order to  
100 capture the forcing of the flow through the Firth it is necessary to accurately simulate the regional tidal  
101 regime. Most of the above studies have focussed on the flow through the entire Pentland Firth, without  
102 focussing specifically on the Inner Sound.

103 In this paper, we provide more detailed information on sediment deposits in the Inner Sound to  
104 the south of Stroma, where the first tidal turbine array is about to be deployed, and, by analysing  
105 measurements and numerical model simulations of local velocity fields, we infer the local sediment  
106 dynamics. Firstly, we describe the planar positions of two hydraulically separated sediments with  
107 respect to the prevailing tidal flow, based on observations by a new multi-frequency sidescan sonar  
108 technique [17]. The sidescan sonar observations are supplemented by video images from a remotely-  
109 operated vehicle (ROV) and multi-beam sonar data. The hydrodynamics of the Inner Sound are  
110 described from a combination of observations from an underway Acoustic Doppler Current Profiler  
111 (ADCP) survey and numerical hydrodynamic modelling. We then speculate that sediment grain size  
112 and shape are primarily responsible for the patterns of sedimentation observed with hydraulic  
113 behaviour of shell fragments differing from that of mineral sediment ([18], [19]). Shell and sand  
114 respond differently to similar hydrodynamic conditions and belong to two different hydraulic  
115 populations [20]. Finally, we use the observed and modelled patterns of current velocity to explain the  
116 observed sediment distributions, and speculate on the potential impacts of a large tidal turbine array on  
117 those distributions. Bedform classifications used in the paper are based on the classification scheme  
118 recommended by the SEPM bedforms and bedding structures research symposium [21].

## 119 **2. Methods**

120

### 121 *2.1 Study Site*

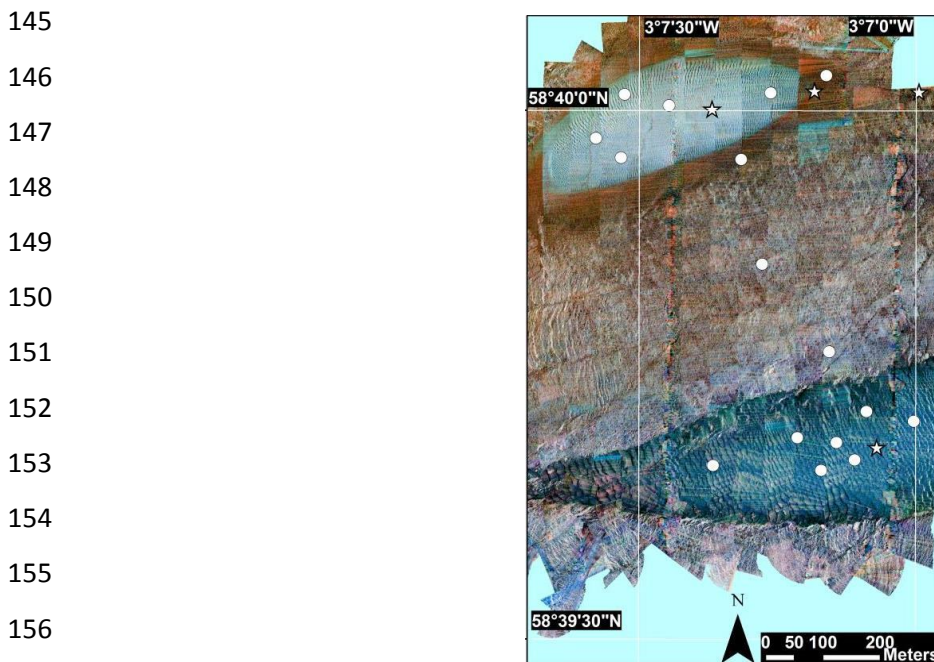
122 Our study site is the Inner Sound between the Island of Stroma and the north coast mainland of  
123 Scotland (Figure 1). This channel forms the southern arm of the Pentland Firth, which lies between the  
124 Orkney Islands and the Scottish mainland and connects the North Sea to the North Atlantic. Water  
125 depths in the Inner Sound reach 40 m in the central channel. Shields et al. [4] described the Pentland  
126 Firth as comprising predominantly of exposed bedrock, but localised sediment deposits are known to

127 exist around Stroma. We conducted acoustic surveys using side-scan sonar, including a novel  
 128 prototype tri-frequency (“colour”) digital sonar, in a focused area within the sound to map the  
 129 sediment banks to the south of Stroma. The acoustic data were ground-truthed using sediment grab and  
 130 a remotely-operated-vehicle (ROV) data from earlier surveys.

131 The survey area was approximately 900 metres by 1200 metres in size. Depths within the study  
 132 area ranged between 10 and 39 metres, with a mean depth of 28 metres (depth derived from multi-  
 133 beam bathymetry [3]), with mostly gentle sloping topography and a tidal range of approximately 4  
 134 metres. The site has been surveyed in the past by a variety of instruments including multi-beam sonar,  
 135 ADCP, ROV and side-scan sonar.

## 136 *2.2 Remotely Operated Vehicle*

137 Data was acquired using a small 6.9m catamaran coastal research vessel ‘Aurora’. Sediment grabs  
 138 and ROV work were undertaken from the vessel. A small ROV was used (Outland Technologies ROV  
 139 1000) which was easily launched from the side of the vessel. A small stills camera was added to the  
 140 ROV and two green lasers to give spatial scale to the still images. Sediment grabs were undertaken by  
 141 hand using a small Van Veen grab. Sediment particle size analysis was undertaken using a standard  
 142 sieve stack and used the Folk and Ward method for sorting categories [22]. Positions of ROV  
 143 snapshots and grab samples used in this paper are shown in Figure 2. Not all grabs were successful  
 144 with only grabs occurring over the two sediment banks successful in recovering a sample.



158 **Figure 2.** Positions of grab samples (shown as circles) and positions of ROV snapshots  
 159 (stars)

### 161 2.3 Side-Scan Sonar

162

163 A prototype multi-frequency side-scan sonar system developed by Kongsberg GeoAcoustics Ltd.  
164 [17], was pole mounted to ‘Aurora’ approximately 1 meter below the hull. The sonar pings at three  
165 frequencies 114, 256 and 410 kHz. The sonar is a basic range-only system and provides no  
166 bathymetric data along trace. The Kongsberg GeoAcoustics Ltd. propriety software ‘GeoTexture’ was  
167 used to process the sonar data. GPS navigation and heading data were provided by a Hemisphere  
168 Vector V110 unit mounted directly above the side scan pole mount.

169 The sonar acoustic data acquired at three ping frequencies constitutes acoustic colour data. These  
170 were mapped onto the optical primary colours in the electromagnetic spectrum for human  
171 visualisation. Acoustic colour sonar is not a new idea, but it has proved difficult to implement. The  
172 sonar backscatter response of the seabed is a function not only of sonar system carrier wave frequency  
173 but also of geometrical spreading and absorption (range); the angular shape of sonar beam functions  
174 and seabed backscatter functions; and sonar vehicle roll and seabed slope. Satisfactory estimates of  
175 the sonar beam function are the key to successfully applying the angular based corrections. A method  
176 to extract sonar beam functions from data affected by sonar vehicle roll is described by Tamsett &  
177 Hogarth [23] and this has provided good estimates of sonar beam functions. Correcting for the non-  
178 seabed effects on sonar amplitude outlined above, and normalising the seabed response for all angles  
179 to that at a reference inclination angle ( $30^\circ$ ), means that acoustic colour becomes a meaningful  
180 property of the seabed. A colour image contains dimensions of information absent in a greyscale  
181 image, and is therefore a richer source of information on the nature of the seabed than a greyscale  
182 image.

183 For the purpose of human visualisation, data at sonar frequencies are mapped to optical primary  
184 colour frequencies such that the colours red, green and blue are seen in proportion to the amplitudes of  
185 the low-, mid- and high-frequency sonar data respectively. Also, optical colour is generated in such a  
186 way that shadow appears white and saturation black; and weakly backscattering seabed as light shades  
187 of colour, and strongly backscattering seabed as dark shades of colour using the negative CMY colour  
188 scheme the details of which are presented elsewhere [17]. Side-scan sonar swaths were plotted on  
189 charts (mosaicked) and overlaid to generate a chart with ensonification (predominantly) to the West,  
190 and then underlain for an image for ensonification to the East. Data were frequency equalised over an  
191 image used as a standard such that the mean seabed colour response over the whole image is an  
192 appropriate mid-shade of grey.

193 Two side-scan surveys were undertaken in the summer of 2015, survey 1 (May, 2015) and survey  
194 2 (June, 2015). Survey 1 was undertaken during flood spring tide conditions and survey 2 undertaken  
195 during ebb spring tides. The trace length was 120 milliseconds (a maximum range and half-swath

196 width of approximately 90 metres). Both surveys were conducted along 15 lines running  
197 approximately North-South spaced at 50 meter intervals. The area of seabed survey was in each case  
198 approximately 900 (N-S) by 1100 (E-W) metres. The time spent at sea was approximately 4 hours,  
199 plus a similar amount of time to mobilise and demobilise the vessel.

200

### 201 *2.5 Acoustic Doppler Current Profiler (ADCP)*

202 Underway ADCP surveys, described by [16], were performed using a 300 KHz Teledyne  
203 Workhorse Sentinel ADCP pole-mounted to the research vessel ‘Aurora’ at approximately 1 meter  
204 below the hull of the vessel, and measured vertical profiles of current speed and direction. Beam 3 was  
205 rotated 45° away from the vessels centreline. Vessel speed was approximately 6 knots when  
206 undertaking the survey. A blanking distance of 2 metres was applied and 12 depth bins, each of 2  
207 metre thickness, selected. The ADCP operated at 2 Hz with single-ping bottom tracking enabled. The  
208 ADCP data were merged with GPS data from an on-board Raymarine GPS system and averaged into  
209 ensembles of 15 seconds. Results from a flood tide survey on 15th April 2009 and an ebb tide survey  
210 on 7th April 2009 are reported here. For more details of the survey technique and data processing  
211 methodology, refer to [16].

212 Subsequent to the underway surveys, two 300 kHz upward-looking Teledyne Workhorse ADCPs  
213 were deployed in the Inner Sound during February – March 2013. Both instruments were deployed in  
214 about 35 m of water to the south of the island of Stroma (Figure 1). The western instrument is denoted  
215 ‘ADCP 1’, the eastern instrument ‘ADCP 2’. The ADCPs sampled at 2 Hz, with data subsequently  
216 averaged into 1-minute ensembles. Bin size was 2 m. Valid data extended from approximately 6.5 m –  
217 30.5 m above the seabed, but have been averaged here into depth-averaged values. Tidal analysis on  
218 the depth-averaged data was performed using the T-TIDE software [24].

219

### 220 *2.6 Sea Surface Height Data*

221 Sea surface height (SSH) data were collected at Scrabster and John O’Groats using an Aanderaa  
222 WLTS 3791A instrument, set to record at 10 minute intervals. Nominal instrument accuracy is 0.02 m.  
223 SSH data at Stroma were collected using a Valeport TideMaster (accuracy 0.01 m), again with a  
224 sampling interval of 10 minutes. Data from the Inner Sound were obtained from a pressure sensor on  
225 the ADCP (see previous section) with 10 minute sampling frequency. Sea level at Wick is routinely  
226 measured for the UK National Tide Gauge Network, part of the National Tidal and Sea Level Facility;  
227 the hourly data used here from February – March 2013 were obtained from the British Oceanographic  
228 Data Centre.

229



## 230 2.7 Hydrodynamic Model

231 The numerical model RiCOM (River and Coastal Ocean Model) is a general-purpose  
 232 hydrodynamics and transport model, which solves the standard Reynolds-averaged Navier-Stokes  
 233 equation (RANS) and the incompressibility condition, applying the hydrostatic and Boussinesq  
 234 approximations. It has been tested on a variety of benchmarks against both analytical and experimental  
 235 data sets (e.g. [25], [26], [27]). The model has been previously used to investigate the inundation risk  
 236 from tsunamis and storm surge on the New Zealand coastline ([26], [28], [29]), and to study tidal  
 237 currents in high energy environments ([30], [31], [32]). Here the model was used to study the highly  
 238 energetic flow through the Pentland Firth.

239 The model grid covered the northern Scottish continental shelf. An unstructured mesh was used,  
 240 with grid resolution increasing from 20 km at the outer boundaries of the model to ~40 m in the Inner  
 241 Sound. The model was forced at the outer boundaries by seven tidal constituents (O1, K1, Q1, M2, S2,  
 242 N2, M4) which were taken from the Oregon State University global tide model [33]. No wind forcing  
 243 was applied and water density was assumed to be constant. Bathymetry was obtained from a variety of  
 244 sources, amalgamating sources of increasing resolution closer to the coast. The model was run in  
 245 depth-averaged mode and was used to simulate the flow through the Pentland Firth over the period  
 246 18th February – 24th March 2013.

247 Results were calibrated against the sea surface height data from Scrabster, Wick, Stroma, John  
 248 O’Groats and the Inner Sound (as described above). Velocity predictions from the model were  
 249 evaluated against the two simultaneous deployments of Acoustic Doppler Current Profilers (ADCPs)  
 250 in the Inner Sound during 2013. More extensive evaluation of the model over the wider domain is  
 251 ongoing.

252 Depth-averaged velocity fields were saved every hour. The maximum velocity that occurred at  
 253 each grid point over the duration of the simulation was also stored. From these maximum velocity  
 254 fields, a maximum bed stress was calculated [34].

$$255 \tau_b = \rho C_D U^2 \quad (1)$$

256 where  $\rho = 1025 \text{ kg m}^{-3}$  is the water density,  $C_D = 0.0025$  is a drag coefficient and  $U$  is the depth-  
 257 averaged velocity. We use the value of  $C_D = 0.0025$  only for the post-simulation calculation of the  
 258 maximum bed stress; during the model calibration process, the frictional drag coefficient is tuned to  
 259 provide the best fit to observations of sea level and velocity.

260

261

## 262 **3. Results**

### 263 *3.1 Side-scan Sonar*

264 Individual frequency channels reveal different details of the seabed (Figure 3). From the merged  
265 colour mosaic image, Figure 3(iv); clear distinctions can be made between material types. Merging the  
266 three frequencies for colour imaging improves classification results in both supervised and  
267 unsupervised classification. Figure 3 shows the results of supervised classification using the same  
268 sample training areas to undertake both classifications on the colour composite image, Figure 3(v) and  
269 single frequencies of which the 114 KHz is shown in Figure 3(vi).

270

271 Two distinct sediment beds are present in the study area and exhibit different acoustic properties.  
272 An oval shaped sediment bank is present in the north of the survey area and a wedge shaped sediment  
273 bank in the southern part of the survey area. Bedrock in the survey area is Devonian sedimentary rock  
274 throughout. Differing acoustic backscattering characteristics from varying amounts of marine growth  
275 results in the differing acoustic responses of the bedrock, with colours from reddish brown (heavy  
276 coverage) to violet (bare rock) seen in the colour mosaic (Figure 2 & Figure 3). Evidence for several  
277 well defined faults can also be detected. A halo of material is seen surrounding the oval bank; the  
278 texture and colouring of the material in the processed side-scan image indicates a different material  
279 than the surrounding bedrock or material composing the oval shaped northern bank.

280

281

282

283

284

285

286

287

288

289

290

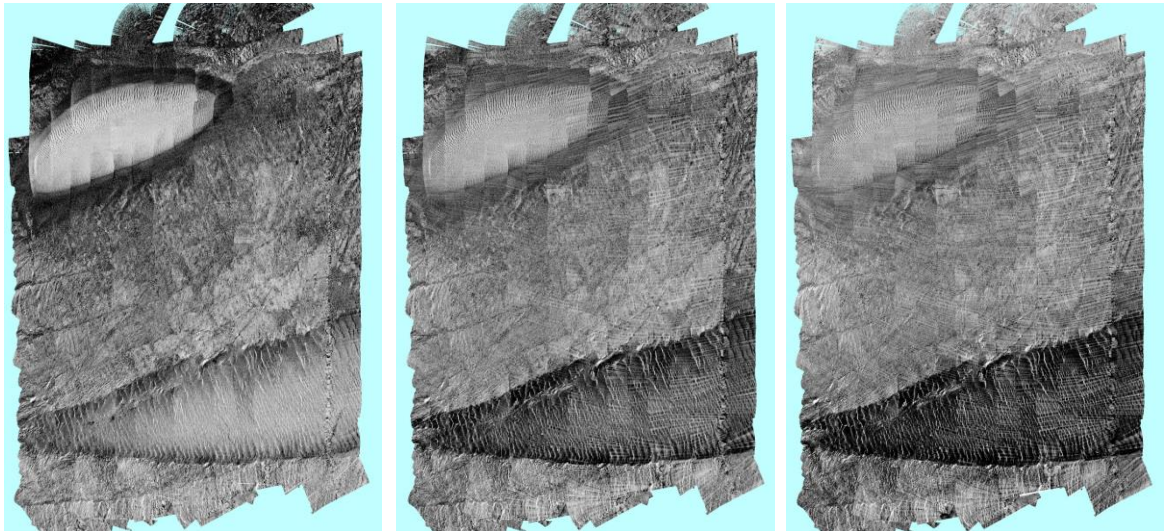
291

292

293

294

295



296

(i) 114 KHz image

(ii) 256 KHz image

(iii) 410 KHz image

297

298

299

300

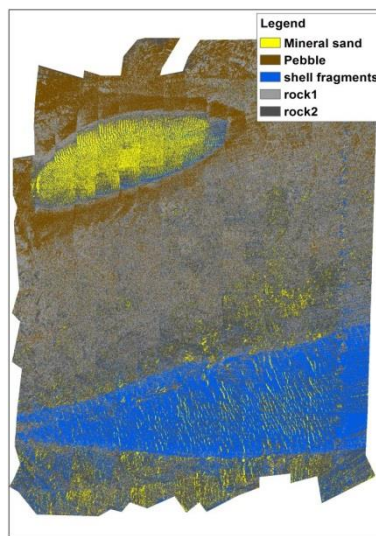
301

302

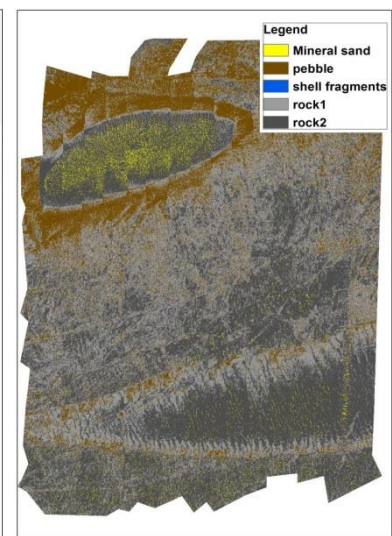
303



(iv) Composite colour



(v) Classified colour



(vi) Classified 114 KHz

304

305

306

307

308

**Figure 3.** Figures respectively showing the frequency channels of 114 (i), 256 (ii) and 410 KHz (iii) of the study area for survey 1. The colour mosaic is shown (iv). Images represent an area of approximately 900 by 1130 metres. (v) Supervised classification of the composite colour image. (vi) Supervised classification of the 114 kHz image.

309

310

311

312

313

314

315

316

The oval shaped sediment bank has a major axis at approximately  $70^{\circ}\text{N}$ . It is approximately 475 metres in length along the major axis and 175 metres in length along the minor axis. The colour composite image from survey 1 (flood tide survey, June 2016) shows superimposed medium sized subaqueous dunes present on the surface of the oval sediment bank in the north of the bank and small sized subaqueous dunes in the south and centre. The dunes on the northern edge have wavelengths between 5 and 7 m and slope to the west, indicating a westerly current direction. On the southern edge the wavelength is smaller, approximately 2-3 m and slope to the east. In the centre of the sediment bank dune wavelengths are smaller with wavelengths of 1-2 metres. The counter-clockwise orientation

317 of the dunes around the bank indicate a circular current or eddy present rotating in a counter-clockwise  
 318 direction during this survey (flood tide).

319 The second side-scan survey was undertaken during spring ebb tides. Comparison between the  
 320 two surveys shows little change in the sediment banks plan shape or position (Figure 4). The plan  
 321 length curvature of some dunes on the northern edge of the oval shaped sand bank show a curve to the  
 322 west or c shaped plan during survey 1 (flood tide) and show a similar pattern in survey 2 (ebb tide,  
 323 Figure 4).

324 However dune profile data from multi-beam survey data (Meygen LTD, 2009, [3]), which was  
 325 undertaken on an ebb-tide indicate that subaqueous dunes on the northern edge slope to the east and  
 326 the small dunes on the southern edge slope to the west, indicating a clockwise current direction around  
 327 the dune when the multi-beam data was collected during ebb tide (Figure 5). The oval shape of this  
 328 sediment bank and its position is related to a tidal eddy, which the side-scan and multibeam survey  
 329 results suggest flows in a counter-clockwise rotation during flood tide and clockwise rotation during  
 330 ebb tide.

331

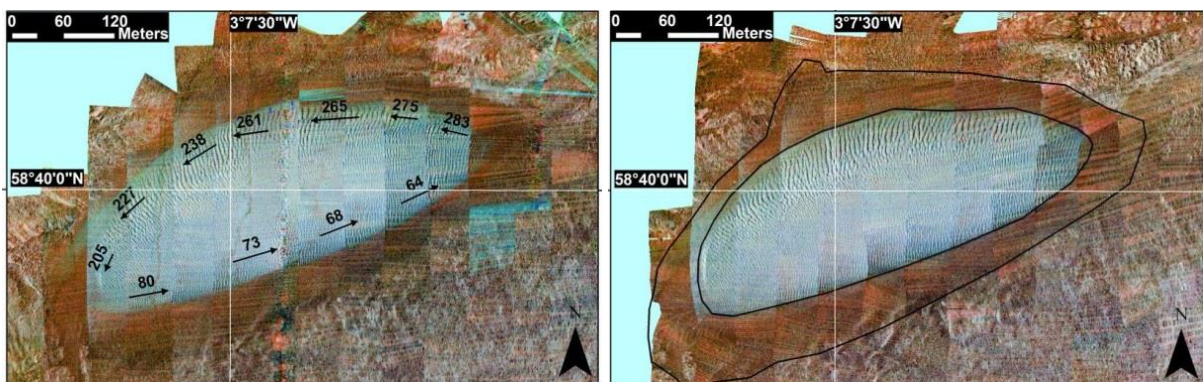
332

333

334

335

336



337

(i)

(ii)

338 **Figure 4.** Dune crest directions on the oval shaped sand bank during spring flood tide,  
 339 June 2015 (i) and ebb tide, May 2015(ii). Little change in dune shape was detected. Arrows  
 340 indicate crest direction for ebb tide (in geographic degrees). Overlain in (ii) black line  
 341 shows dune outline position and position of halo surrounding dune from June survey in (i).

342

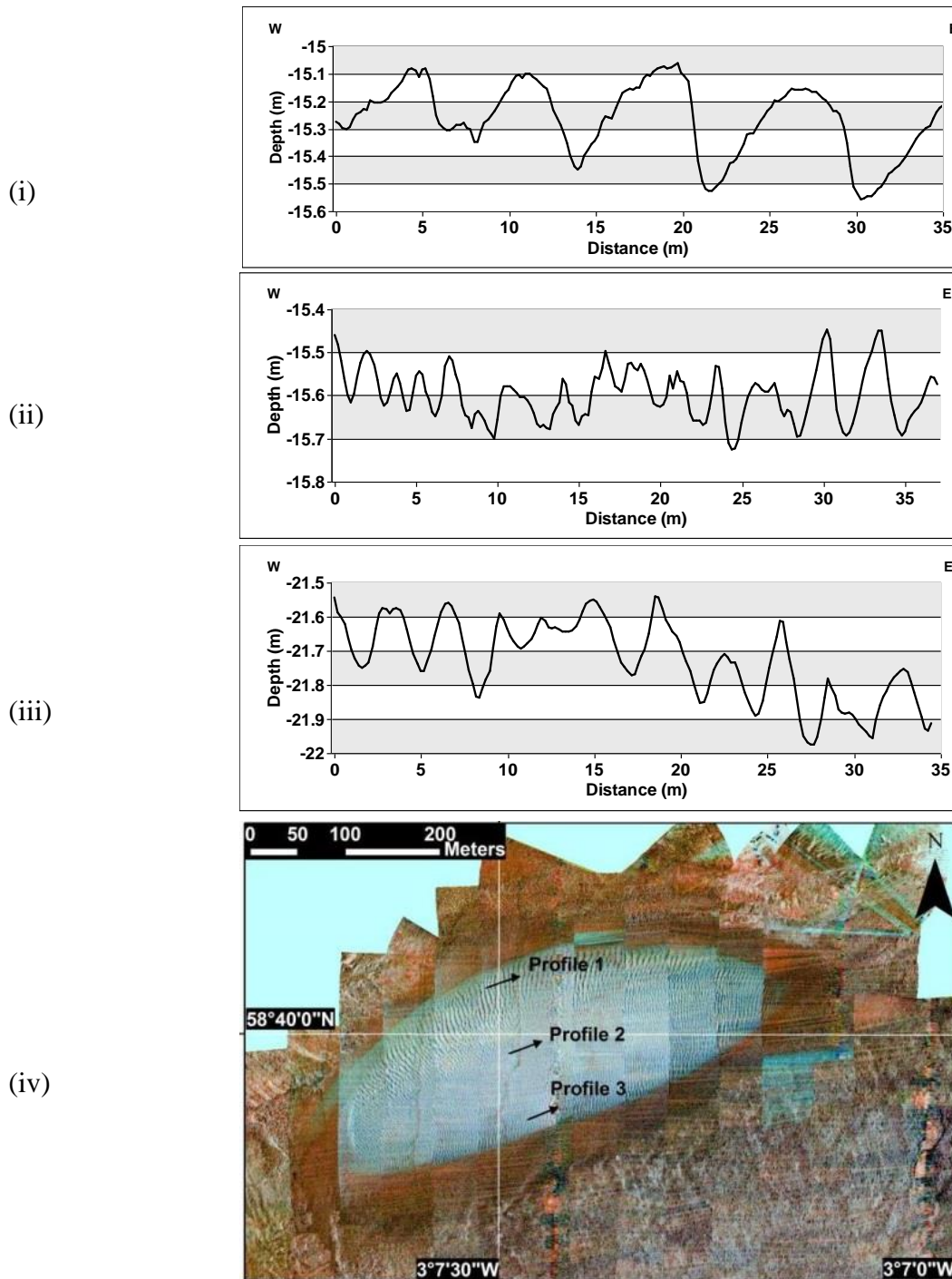
343

344

345

346





368 **Figure 5.** (iv) Position of dune profiles along three sections on the oval dune overlain on  
 369 survey 2 (June, 2015). Profile bathymetric data from multi-beam data collected during the  
 370 ebb phase (2009, [3] ). (i) Profile 1 shows sand dunes with 40 cm amplitude and up to 7 m  
 371 wavelength; (ii) Profile 2 showing small dunes in the centre of the oval dune, Amplitudes  
 372 of ~10 cm and 1 – 2 m wavelength. (iii) Profile 3 showing smaller sand dunes on the  
 373 southern edge of the oval sediment bank. Amplitudes of 20 cm and wavelength of 2-3 m

374

375 The southern wedge shaped sediment bank is not mapped in its entirety, but multi-beam survey  
 376 data show it to be a minimum of 2 km in length, being approximately 450 metres in width at the  
 377 eastern side of the Inner Sound [3]. This feature eventually forms a wider formation out-with the sound  
 378 and study area to the east which has not yet been fully mapped.

379 The largest dunes superimposed on the southern wedge shaped sediment bank are found on its  
 380 northern edge with wavelengths varying between 10 and 30 metres. On its southern side dunes have  
 381 crests between 10-15 metres. Smaller dunes exist in the centre of the formation with wavelengths of  
 382 approximately 5 metres.

383 The wedge shaped southern sediment bank shows a change in direction of the dune slope  
 384 orientation with crests sloping toward approximately  $250^{\circ}\text{N}$  during survey 1 (ebb tide, June 2016) and  
 385 toward  $70^{\circ}\text{N}$  during survey 2 (flood tide May 2016, Figure 5). No change was observed in the plan  
 386 position of the wedge shaped bank in the two side-scan surveys undertaken. This is also the case when  
 387 compared to a much earlier multi-beam surveys obtained by Meygen LTD in September 2009 [3].

388

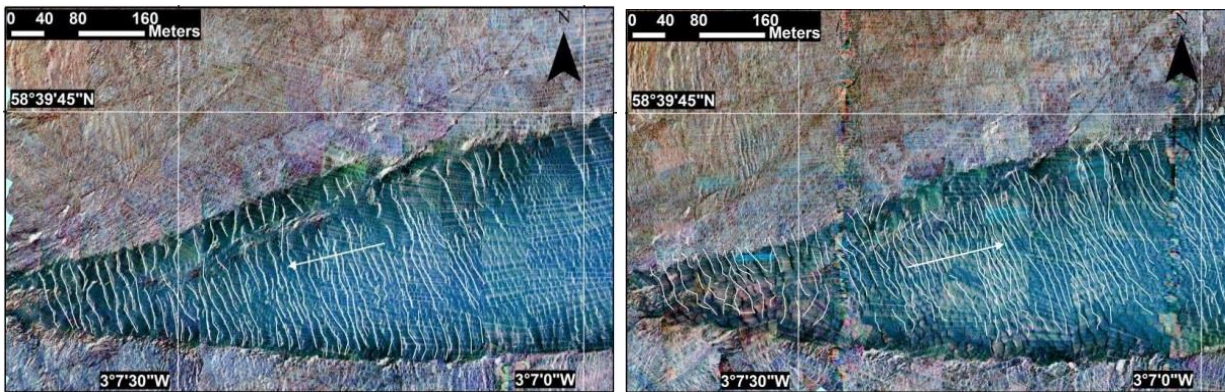
389

390

391

392

393



394

(i)

(ii)

395 **Figure 6.** Side scan mosaic showing shell bed dune orientation during spring ebb tide (i)  
 396 and spring flood tide (ii).

397

398 Seabed profiles obtained from the multi-beam survey show similar dune wavelengths as the side-  
 399 scan surveys (Figures 5 & 7). Figure 7 illustrates the wavelengths and amplitudes of the sand dunes on  
 400 the northern edge of the wedge shaped sediment bank. The multi-beam survey shows little difference,  
 401 with wavelengths on the surface of the sediment bank compared with the side-scan surveys presented  
 402 here.

403

404

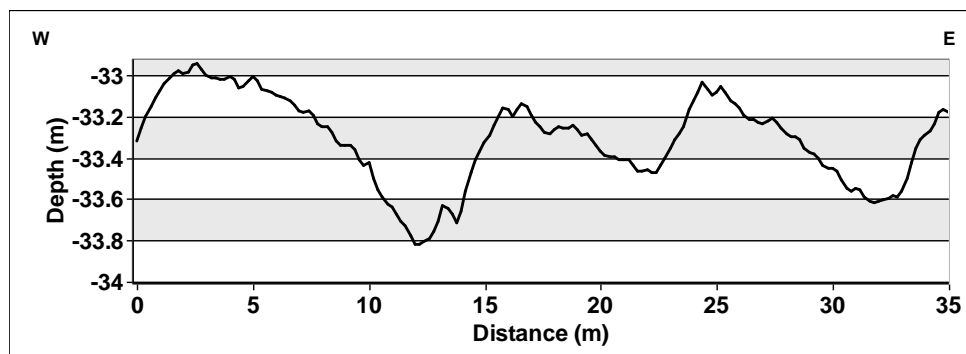
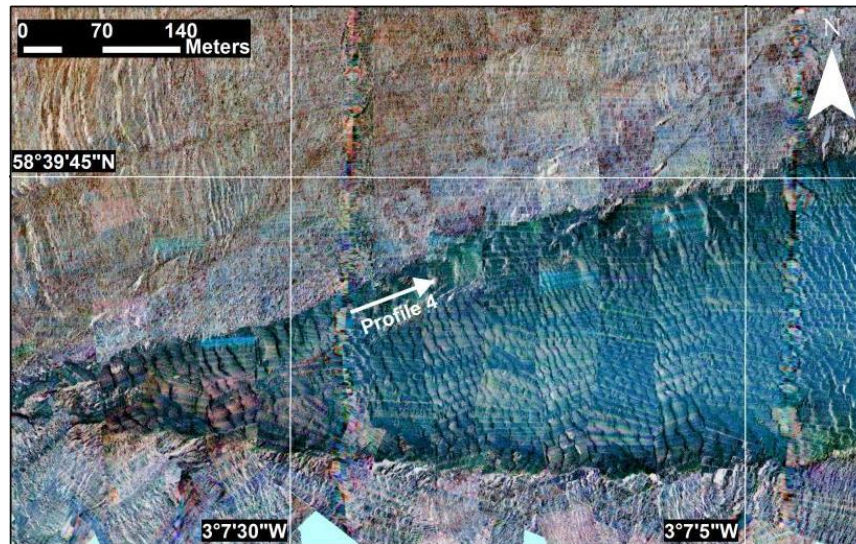


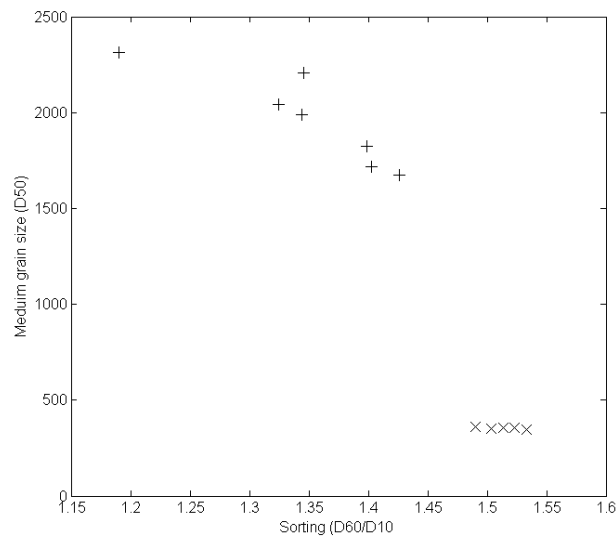
**Figure 7.** (Top) Profile from the multi-beam survey 2 (June, 2016, ebb tide) taken on the wedge shaped sediment bank, arrow indicates start and stop of profile line. (Bottom) Profile 4 showing large sand dune formation on the northern edge of the wedge shaped sediment bank. Wavelengths of >10m and amplitudes up to 1 m.

### 3.2 ROV and Sediment Grabs

Small sediment grab samples were taken and standard particle size analysis undertaken. Samples from the northern sediment bank were found to be unimodal, moderately well sorted medium grained sand, with a mean grain size (D50) of 354.18 $\mu$ m taken from an average of 5 samples (Figure 8).

Sediment samples recovered from the wedge shaped sediment bank showed the material to be almost exclusively fragmented carbonate shell (0.1 % medium sand present average of all samples). There are other such examples of biogenic shell banks surrounding the Pentland Firth area and have been found to be composed almost exclusively of carbonate shell fragments ([11], [12], [13]). Standard particle analysis is not well suited to this material due to the non-spherical nature of the shell

425 fragments. However particle size analysis showed it to be very coarse sand to fine gravel texturally  
 426 with a mean grain size of 1966  $\mu\text{m}$  from an average of 7 samples.



427

428 **Figure 8.** Grain size distributions for the shell fragments (+) and medium grain sand (x).

429 ROV still images show the sediment banks *in situ*; the green dots present on the image are laser  
 430 points from the ROV indicating a scale of approximately 20 cm. ROV surveys revealed that the halo of  
 431 material evident in side-scan sonar imagery surrounding the oval shaped sediment bank was composed  
 432 of smoothed rounded rock pebbles. Pebbles were estimated to be between 4 and 6 cm in diameter on  
 433 average with larger pebbles present (up to 15 cm diameter). Between the pebbles, shell fragments  
 434 similar to those found in the southern wedge shaped bank were found (Figure 9). Kelp fronds are  
 435 present in areas of the halo growing on the pebbles.

436

437

438

439

440

441

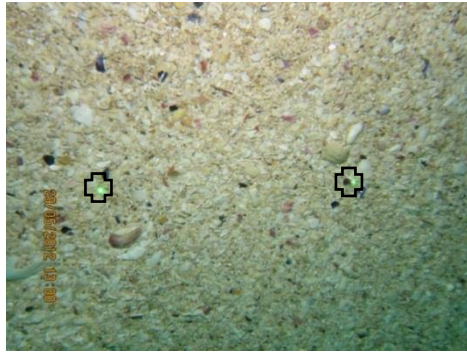
442

443

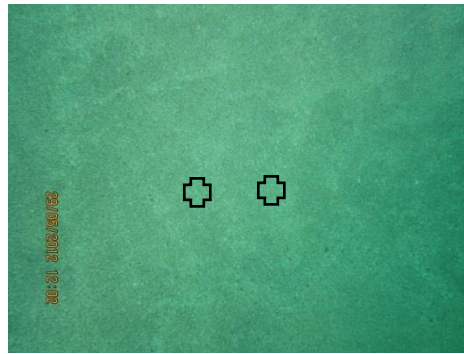
444



445  
446  
447  
448  
449

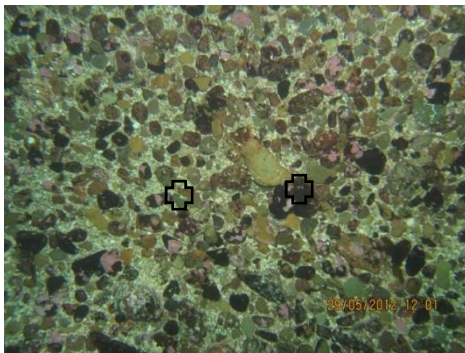


(i)

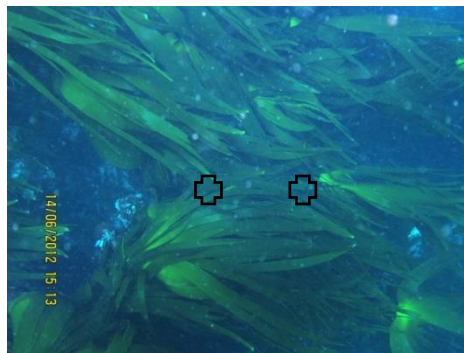


(ii)

451  
452  
453  
454  
455



(iii)



(iv)

457  
458  
459  
460  
461

**Figure 9.** ROV images showing shell material from the wedge shaped sediment bank (i) and medium grained mineral sand from the oval shaped bank in the north of the study area (ii). Pebble halo surrounding oval shaped sediment bank to the north of the study area (iii) and kelp covered bedrock (iv). Markers show position of laser markers showing approximate 20 cm scale. (Laser markers only visible in high resolution image).

462  
463

### 3.3 Acoustic Doppler Current Profiler (ADCP)

464  
465  
466  
467  
468  
469  
470  
471

The ADCP survey revealed the area of fastest flow during flood tide lay within the southern central section of the channel, on the southern edge of the wedge shaped shell bank, with current speeds reaching almost  $3 \text{ m s}^{-1}$  during this survey. Currents were much weaker in the northern part of the channel, but the ADCP survey did not extend into the bay on the southern coast of Stroma (Figure 9). The ebb tide currents were strongest at the western end of the channel, again reaching speeds of almost  $3 \text{ m s}^{-1}$ . In the central channel, ebb tide currents were much weaker than during flood tide, but this is mostly explained by the smaller tidal range at the time of the ebb tide survey.

472  
473

The velocity profile in the vicinity of the shell bank in the central channel demonstrated that speeds were greater than  $2 \text{ m s}^{-1}$  but less than  $3.5 \text{ m s}^{-1}$ . The material in the shell banks is therefore

474 resistant to relatively high flow speeds. Current speeds along the southern edge of the shell bank  
475 increase with velocities exceeding 3.5 m s<sup>-1</sup>. At peak spring tides, instantaneous flow speeds in the  
476 central channel 6 m s<sup>-1</sup> have been recorded [15].

477

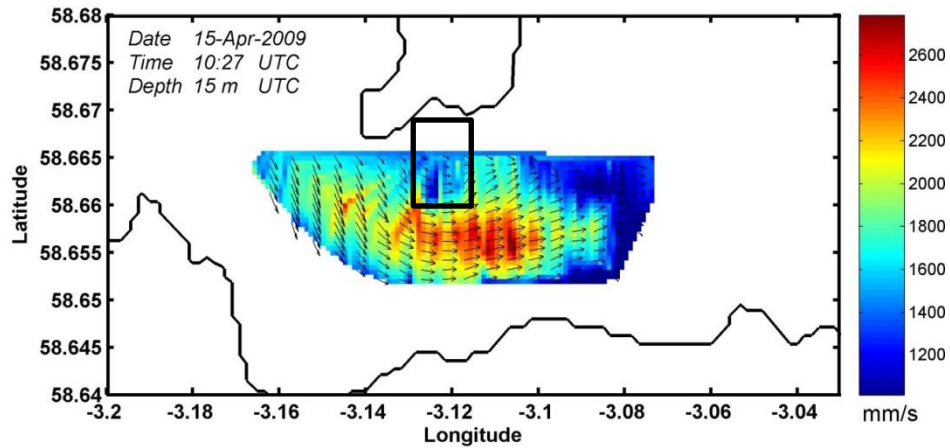
### 478 *3.4 Hydrodynamic Modelling*

479

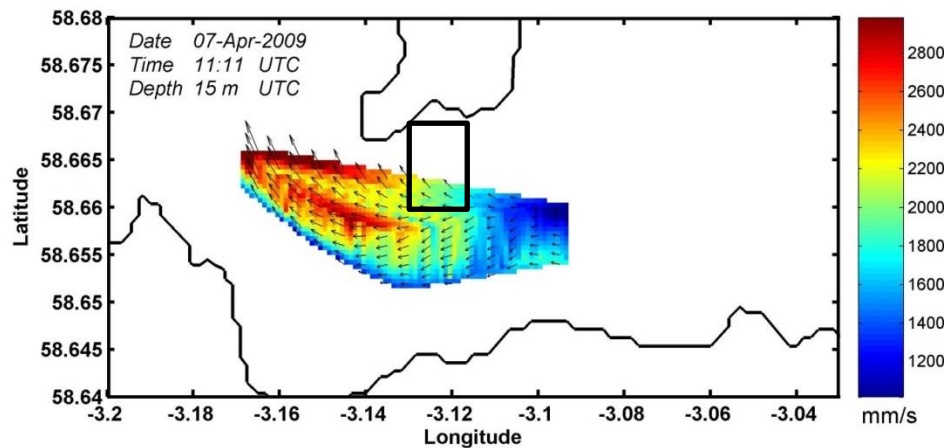
480 The hydrodynamic model satisfactorily reproduced the tide at tide gauge locations around the  
481 northern Scotland coastline including both ends of the Pentland Firth (Table 1), a fundamental  
482 requirement since currents in the Firth are largely driven by sea level pressure gradients [15]. We  
483 varied the frictional drag coefficient,  $CD$ , over an order of magnitude from  $CD = 0.001$  to  $CD = 0.01$   
484 and found best agreement with the data with mid-range values. The model results reported here are  
485 from the simulation with  $CD = 0.004$ . Modelled tidal height constituent amplitudes were typically  
486 within  $\pm 0.04$  m, and phases within  $10^\circ$ .

487 Figure 10 shows flood (i) and ebb (ii) underway ADCP measurements which show similarity to  
488 the modelled output (Figure 11).

489



(i)



(ii)

494 **Figure 10:** ADCP observations of tidal currents during flood (i) and ebb (ii) tides, from  
 495 April 2009. The tidal currents were corrected for temporal distortion using a method  
 496 described in [12], resulting in currents estimated at mid-track time. Study area marked  
 497 with black rectangle.

498 Comparison with moored ADCP data also showed similarity in the magnitudes and phases of  
 499 velocity for the principal tidal constituents (Table 2). The  $M_2$  tidal constituent dominated both the  
 500 regional tides and particularly the tidal currents in the Inner Sound, being 2.5 times stronger than the  
 501 next largest constituent  $S_2$  (Table 2).

502

503

504

505 **Table 1.** Modelled and observed amplitude (m) and phase ( $^{\circ}$ ) of the tidal height for the five principal  
 506 tidal constituents at five locations around the Pentland Firth (see Fig. 1).

Site		$O_1$		$K_1$		$N_2$		$M_2$		$S_2$	
Scrabster	Gauge	0.10	351	0.14	142	0.29	219	1.36	244	0.51	277
	Model	0.09	10	0.13	143	0.29	218	1.36	243	0.51	277
ADCP 2	Gauge	0.11	7	0.09	170	0.16	250	0.94	279	0.43	317
	Model	0.10	17	0.12	156	0.20	250	0.97	274	0.34	310
Stroma	Gauge	0.11	1	0.13	176	0.17	249	0.89	282	0.36	325
	Model	0.10	18	0.12	157	0.18	254	0.92	278	0.32	314
John O'Groats	Gauge	0.10	8	0.11	161	0.18	257	0.83	284	0.28	320
	Model	0.09	23	0.11	161	0.18	261	0.93	284	0.31	321
Wick	Gauge	0.11	29	0.10	176	0.18	298	0.96	322	0.32	1
	Model	0.09	34	0.11	173	0.19	291	0.97	312	0.33	351

507

508 **Table 2.** Modelled and observed amplitude ( $m\ s^{-1}$ ) and phase ( $^{\circ}$ ) of the tidal velocities for the principal  
 509 tidal constituents.

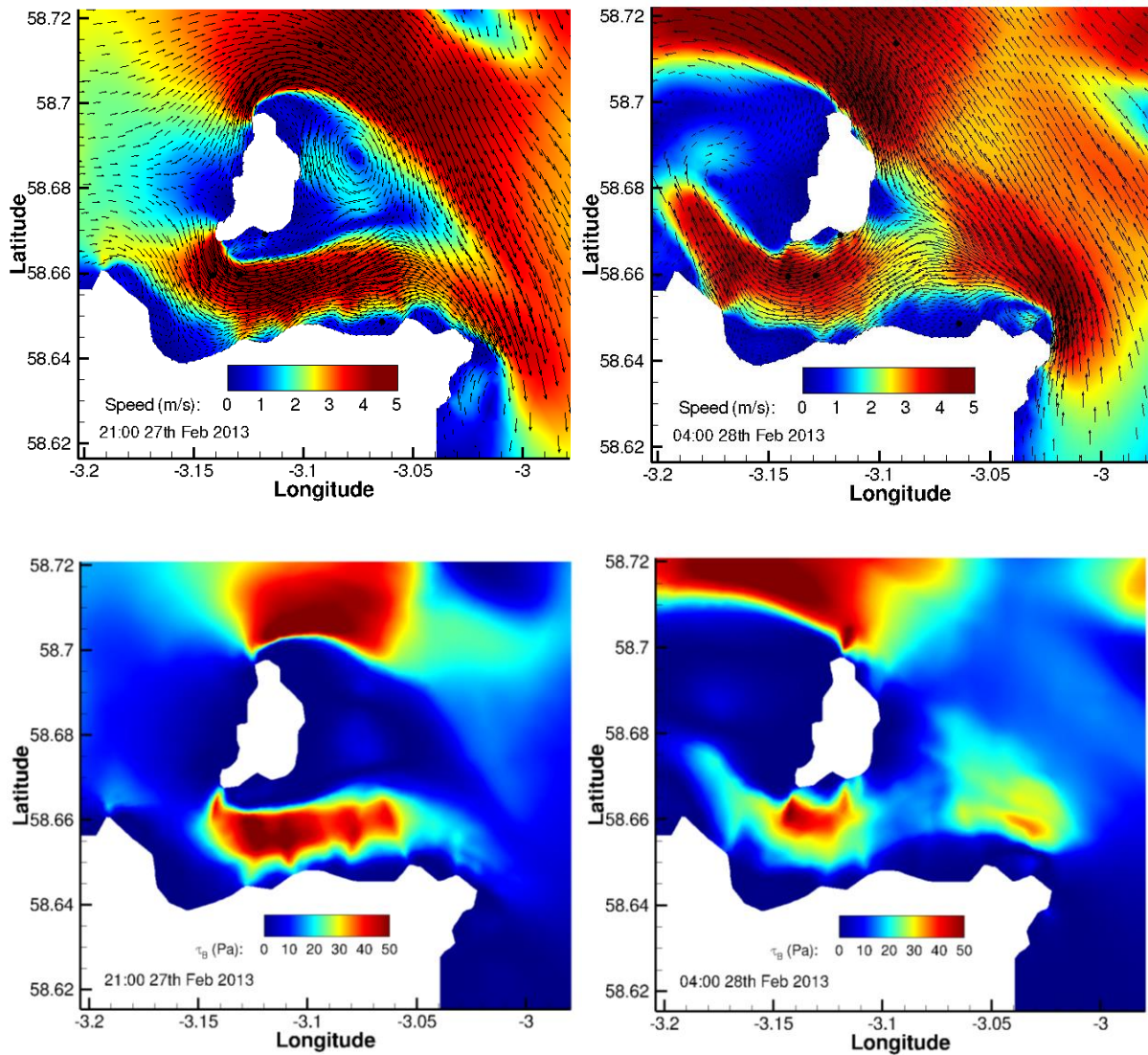
Site		$O_1$		$K_1$		$N_2$		$M_2$		$S_2$	
ADCP 1	Obs	0.11	285	0.08	130	0.44	211	2.59	240	1.09	278
	Model	0.05	324	0.11	92	0.48	203	2.70	239	0.85	269
ADCP 2	Obs	0.09	281	0.07	111	0.48	202	2.92	239	1.17	274
	Model	0.05	322	0.11	93	0.52	203	2.82	238	0.91	269

510

511 Modelled velocity fields show flow separation occurring at the northern and southern headlands of  
 512 Stroma on the flood tide (Figure 11), with counter-eddies forming to the east. A large eddy attached to  
 513 the northern stream forms in the lee of Stroma, whereas a smaller counter-eddy is trapped in the bay on  
 514 the south coast of Stroma where the oval shaped sand dune is located. The model snapshot clearly  
 515 illustrates the blocking effect of Stroma directing the tidal stream through the Inner Sound channel,  
 516 with the core flood tidal stream steered southward into the centre of the channel. The shell bank is  
 517 located along the northern periphery of the strongest flood currents. During the ebb tide, the model  
 518 shows the strongest flow occurs closer to Stroma and at the western end of the channel, with the  
 519 currents south of Stroma being weaker than during the flood tide. At the location of the flood tide  
 520 eddy, the flow is now partly shadowed by the headland to the east, with weaker currents evident. At

521 the start of the ebb tide, the large eddy east of Stroma is swept north-westwards into the main Pentland  
 522 Firth channel.

523



524

525

526 **Figure 11:** Model-predicted depth-averaged currents on a spring flood (top left) and  
 527 spring ebb (top right) on 27<sup>th</sup> – 28<sup>th</sup> February 2013. Current vectors ( $\text{m s}^{-1}$ ) are overlain  
 528 on the coloured current speed ( $\text{m s}^{-1}$ ). The bed shear stress (Pa) for the corresponding  
 529 flood (bottom left) and ebb (bottom right) tides are calculated using Equation (1).

530

531 Bed shear stress on flood and ebb tides were calculated using Equation (1). On flood tides,  
 532 modelled bed stress values increased from about 0.5 Pa off the southern coast of Stroma to more than  
 533 50 Pa in the central channel (Figure 11). On the ebb tide, the area of low values was confined more  
 534 closely to the Stroma coast, and values were not so high in the central channel south of Stroma,

535 peaking to the south-west of the island. High values ( $> 50$  Pa) are evident to the north of the island on  
536 both flood and ebb tides.

537

## 538 **4. Discussion**

### 539 *4.1 Hydrodynamics of the Inner Sound*

540 Both the observations and the hydrodynamic modelling presented here illustrate the asymmetry in  
541 the tidal current regime through the Inner Sound. Flood tide currents entering the Sound from the west,  
542 are diverted southward into the centre of the channel by the headland at the south-western extremity of  
543 Stroma. The main flow is accelerated around the headland, forming a stream about 1 km wide through  
544 the channel wherein current speeds at spring tides regularly exceed  $4.5 \text{ m s}^{-1}$  (and have been recorded  
545 at up to  $6 \text{ m s}^{-1}$ ) to the south of Stroma. Previously published ADCP data [16] show similar features.  
546 Modelling results suggest a trapped counter-eddy develops in the bay on the south coast of Stroma, at  
547 the location where a persistent sand bank was observed. On the ebb tide, flows accelerate through the  
548 channel, with fastest speeds occurring to the south-west of Stroma. The ebb stream through the Inner  
549 Sound is shifted slightly north compared to the flood stream, since the headland at the south-east  
550 corner of Stroma does not protrude so far into the channel. In the central Inner Sound, current speeds  
551 during ebb tide are significantly less than during flood, and are orientated to the south-west rather than  
552 directly west. Maximum bed stress in the channel is therefore determined predominantly by the flood  
553 tide velocity field.

554 Predicted bed stress in the Sound during flood tide ranged from about 0.5 Pa beneath the trapped  
555 eddy in the bay on the south coast of Stroma to values exceeding 50 Pa in the central channel and  
556 higher ( $> 60$  Pa) off headlands and in the main Pentland Firth channel north of Stroma. With flood tide  
557 bed stress values less than 1 Pa, we might expect to find medium or coarse sand beneath the eddy [8];  
558 the sonar observations reported here, confirming the presence of an oval-shaped bank of medium sand  
559 in that location, therefore provide corroborating evidence for the numerical model predictions and,  
560 conversely, help us understand the persistent nature of the sandbank. Model simulations reveal that the  
561 flood tide counter-eddy in the bay is a persistent feature and that the bank is also protected from the  
562 ebb tide currents by the headland to the east.

563 To the south of the eddy, bed stresses increase rapidly into the central channel. Bed stress values  
564 of up to 25 Pa might allow coarse gravel sediments to persist [8]. The wedge-shaped bank observed  
565 by the sonar certainly lies in an area where bed stress values can be relatively high; possible reasons  
566 for the presence of this bank are discussed in the following sections.



## 567 4.2 Grain settling velocity and entrainment

568 A limitation of side-scan sonar with the frequencies used here (114-410 KHz), is that only the  
 569 surface of the material is imaged. However after extensive ROV video surveys combined with  
 570 sediment grabs, only shell fragments were observed to compose the wedge shaped southern bank. It is  
 571 known that other such banks exist in the local region ([11], [12], [13]), an example of which is the  
 572 Sandy Riddle, located approximately 13 km to the east composed almost exclusively of carbonate shell  
 573 fragments [12]. Based on the ROV evidence, sample grab and surface sonar reflectivity of the bank it  
 574 is expected the bulk composition of the southern wedge shaped bank is also carbonate shell fragments.

575 With this premise the composition and position of this bank can be attributed to the size, shape  
 576 and density of the shell fragments. Settling velocity,  $\omega_s$ , can be calculated by differing empirical  
 577 expressions in which the calculation of drag coefficient as a function of fluid and grain properties  
 578 differs. Ferguson and Church [35] provide a simple expression which serves well for a variety of  
 579 sediments:

$$580 \quad \omega_s = \frac{RgD^2}{C_1v+(0.75C_2 RgD^3)^{\frac{1}{2}}} \quad (2)$$

581 where R is the submerged specific gravity, g is the acceleration due to gravity, v is the kinematic  
 582 viscosity, D is the grain diameter in m, and C<sub>1</sub> is a constant with a theoretical value of 18 and  
 583 represents the smoothness of the grains. C<sub>2</sub> is the constant asymptotic value of the drag coefficient.  
 584 The drag coefficient is 1 for a spherical grain, natural mineralogical sediment have a value ranging  
 585 from 0.8 to 1.15 dependent on shape (Table 3).

586

587 **Table 3.** Smoothness and shape drag coefficient values for Equation 2

Constant	Smooth Spheres	Natural grains: Sieve diametres	Natural grains: Nominal diametres
C <sub>1</sub>	18	20	24
C <sub>2</sub>	0.4	1	1.1

588

589 The important aspect to all such equations is the behaviour of a particle in a fluid in relation to the  
 590 particles density and shape and most such equations are based on a near spherical particle such as  
 591 natural mineralogical sand. Shell is not spherical or a near-spherical particle with near-spherical  
 592 particles showing preferential transport in comparison [36]. Broken shell consists of a large diameter

593 grain which is very thin in cross section [18]. This type of particle will have a larger drag coefficient  
594 when settling due to the large cross section area exposed to the upward force of the fluid, or a large lift  
595 surface [37]. The opposite is true once the shell material is settled, shell material generally settles on  
596 the side with the largest surface area, and the thin cross-section exposed to the current. In this  
597 configuration the drag coefficient is now much lower than natural sediment. Studies have suggested  
598 that drag coefficients for whole shells are as low as 0.09 or less [18]. A much lower drag coefficient  
599 requires a faster current to entrain the shell fragments, with bedforms having resistance to high flow  
600 when in a structured bed [37]. However the shape of shell particles makes it difficult to numerically  
601 predict the hydrodynamic response of the particles ([18], [19]). The initial movement of non-spherical  
602 grains is further complicated by turbulent flow. A standard method to quantitatively identify the  
603 inception of grain motion is the Shields parameter [38], however no universal method for all sediment  
604 types has yet been developed [39], with many researchers applying corrections with respect to specific  
605 sediment types ([40], [19]).

606 No information is available on the deposition rate on either sediment bank however similar shell  
607 banks within the geographical area have been estimated to have accumulation rates of 540 g/m<sup>2</sup> yr. or  
608 67 cm/1,000 yr. [11]. The shell material is provided by organisms growing on the local shelf which is  
609 thought to be of low diversity and abundance ([12], [13]).

610 It is postulated that the southern wedge shaped sediment bank in the side-scan surveys can be  
611 viewed as a lag deposit composed primarily of carbonate shell fragments [20]. Mineral sand is present  
612 in very low quantities in all grab samples with carbonate shell fragments composing >99% of the  
613 sediment, it is likely mineral medium grained sand is swept through the channel or captured in the  
614 eddy formation and deposited on the medium grained sediment bank to the south of Stroma.

#### 615 *4.3 Inferred sediment dynamics*

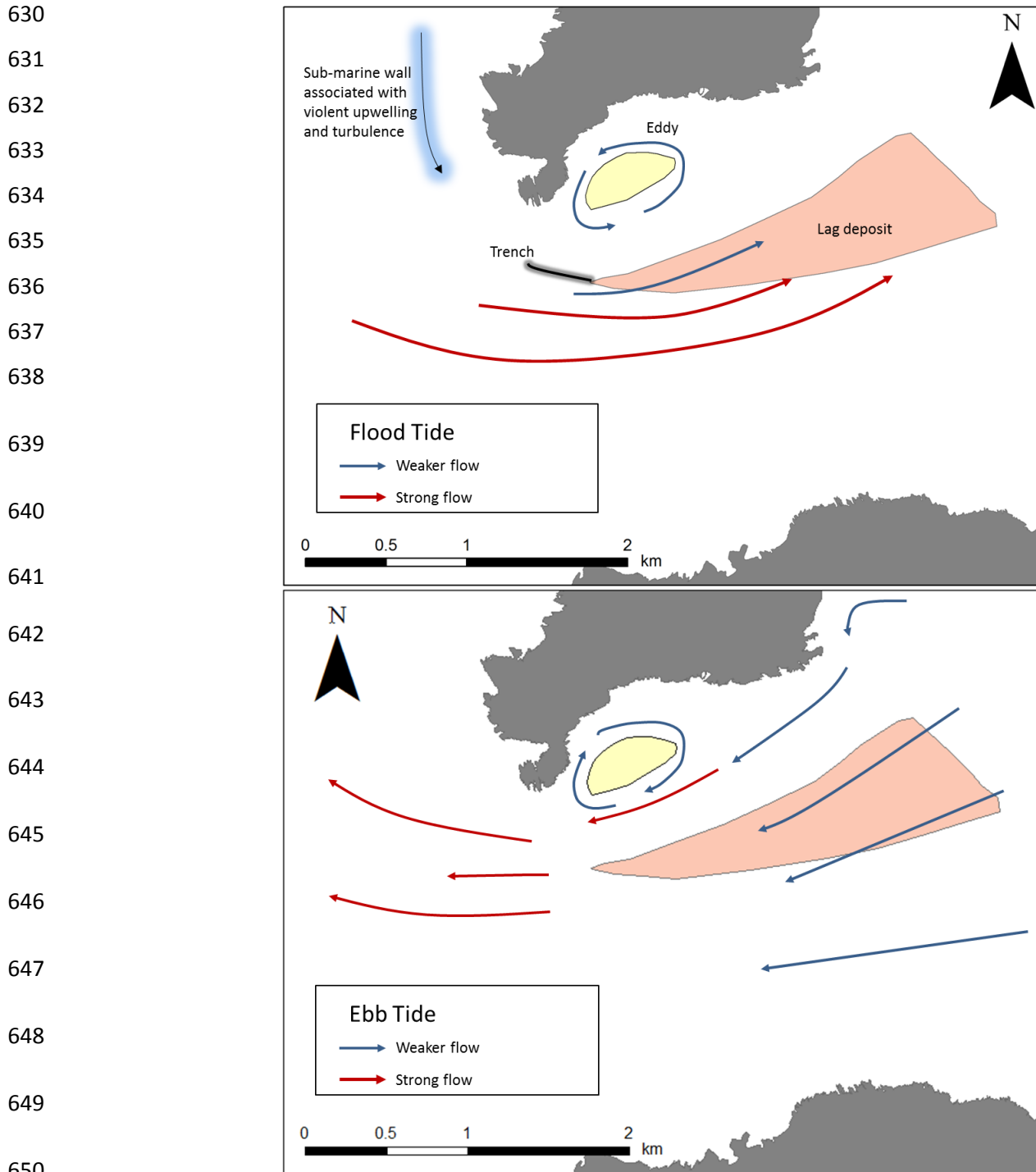
616 From available data a simple interpretation of the pattern of sediment within the Inner Sound can  
617 be speculated (Figure 12). The two sediment bodies present within the study area represent two  
618 different hydraulic populations, in place due to the pattern of tidal currents, bathymetry, sediment  
619 availability and sediment type. The difference in drag behaviour between natural sand and the shell  
620 fragments is an important factor in the observed sediment distribution.

621

622 Shell fragments can be seen in the water column visually and a possible local source for the shell  
623 to become entrained is near a submarine ledge which exists on the eastern side of Stroma. From ROV  
624 footage it is estimated this feature is an almost vertical wall from approximately 15 metres or more in  
625 depth to less than 5 metres depth at spring low tide (chart datum). During flood tide this feature causes



626 powerful turbulence with vortexes, explosive kolk-boil which erupt on the surface running along the  
 627 edge of the submarine ledge, this is a source of initial shell entrainment into the channel. Shell  
 628 fragments are transported into the channel by bedload and suspended transport then deposited outside  
 629 the main current flow during slack tide in reduced current speeds (Figure 12).



651 **Figure 12:** Inferred sediment dynamics during flood (top) and ebb (bottom) tides. The  
 652 yellow oval bank is medium grained sand whilst the pink wedge shaped bank is carbonate  
 653 shell.

654 Finer grained natural mineral sediment is not able to settle until it is carried into a clam area and  
655 deposited on the centre of the eddy which exists to the east of the rocky prominence on the south side  
656 of the island. This sand bank is then shaped by the eddy feature during flood tide. During ebb tide the  
657 flow is not sufficient for entrainment of the shell fragments once settled with only surface remodelling  
658 occurring. Subaqueous dune direction change is evident between surveys taken during flood tide and  
659 ebb tide.

660 The shell fragments form a bedform which is resistant to high current flow although surface re-  
661 modelling occurs during different tidal phases. Tidal asymmetry is not sufficient to alter the plan  
662 position of the bank by bedload transport alone. From the inferred mechanics of deposition it is  
663 speculated that the sediment banks present in the inner sound are not transient features but have been  
664 locked in place by the pattern of current flow. The shell gravel bank and medium grained sand bank  
665 may be sensitive to change in local hydrodynamics, in particular plan position of the shell bank.  
666 Settling velocities and entrainment velocities of the shell fragments are of importance when  
667 considering future sediment modelling of this region, in particular under turbulent flow.

668

#### 669 *4.4 Implications for Tidal Energy Extraction*

670 The Inner Sound is the site of the likely first tidal turbine array to be deployed in the world [3],  
671 with installation commencing in 2016. Initially four turbines will be deployed, followed by, in a  
672 phased deployment programme, 82 more and eventually up to 279 turbines in total. Total energy  
673 generation is expected to reach up to 398 MW. Extracting energy from tidal systems is very likely to  
674 have effects on the sediment dynamics of the local area ([6], [7], [8], [9]). As the deployment of  
675 turbines in the Inner Sound proceeds, we can therefore expect to see changing patterns of sediment  
676 deposition and erosion in the Inner Sound, with evolving seabed sediment distributions. As described  
677 above, the currently observed sediment distributions are dependent on the prevailing hydrodynamics,  
678 and the shell bank in particular is sited in a narrow band of current conditions. An array of turbines to  
679 the south in the main tidal flow is likely to partially divert the flow around the array, due to partial  
680 blocking, and enhance the current speeds around the sides. It seems plausible, therefore that the shell  
681 bank may ultimately be eroded or, more likely, relocated by the changing hydrodynamics.

682 Monitoring the evolution of these sediment features following deployment of the turbines may be  
683 of scientific interest, in particular, by comparing numerical predictions with ongoing observations.  
684 This knowledge will be of value for regulators and the marine energy industry itself, in assessing  
685 potential impacts of proposed tidal arrays elsewhere in the UK and abroad. And whilst the sand and  
686 shell banks described here are small features, changes to the large scale sediment dynamics of the  
687 region may have knock-on effects on downstream benthic habitats [10], including marine protected  
688 areas, which often contain sessile filter feeding organisms dependent on suspended sediment transport

689 for food. To understand the potential effects of wider marine energy development in the coastal zone  
690 over the coming years and decades, therefore requires fully calibrated and tested hydrodynamic and  
691 sediment transport models. Monitoring of sediment distributions in areas such as the Inner Sound will  
692 provide a valuable observational resource to test and develop those models.

693

## 694 **5. Conclusions**

695 The pattern and strength of tidal current flow within the Inner Sound has sorted the available  
696 sediment into two distinct sediment banks which have likely been locked in place for a significant time  
697 period and developed throughout the Holocene since sea level rise allowed.

698 Based on studies of similar sites in the region, deposition rates for both banks are expected to be  
699 low with sediment being reworked on the banks by tidal flow. The shape and density of the shell  
700 fragments affect drag; once deposited the bedform is highly resistant to high current velocities.  
701 Modelling of the transport of shell fragments will help in assessing the likely impact of change in  
702 hydrodynamics to the banks; however the difficulty remains in modelling the behaviour of irregularly  
703 shaped particles in turbulent flow.

704 Multi-frequency sidescan sonar and the introduction of colour to the processed imagery has  
705 improved classification of the seabed as compared with single frequency data.

706

## 707 **Acknowledgments**

708 Contribution to project TURNKEY (Transforming Underutilised Renewable Natural Resource  
709 into Key Energy Yields; project 2013-1/279) of the Atlantic Area Transnational Cooperation  
710 Programme financed by the European Regional Development Fund (ERDF). Thanks to Meygen Ltd.  
711 for supplying multi-beam data used in this paper, and to Jon Hardwick of the University of Exeter for  
712 providing us with the ADCP data from site ADCP 1 for model calibration. Sea level data from Wick  
713 were obtained from the British Oceanographic Data Centre. We are grateful to Roy Walters for  
714 providing his model code and his help in setting up the model of the Pentland Firth. We thank two  
715 anonymous reviewers for their suggestions which much improved the paper.

716

## 717 **Author Contributions**

718 Jason McIlvenny led the field work, undertook the data analysis and wrote the paper; Duncan Tamsett  
719 led the colour sonar development, wrote the GeoTexture software used to process the sonar data, participated  
720 in the field work, analysed the colour sonar data and co-wrote the paper; Philip Gillibrand undertook the

721 modelling work and co-wrote the paper; Lonneke Goddijn-Murphy undertook the underway ADCP survey,  
722 analysed the data and edited the manuscript.

### 723 **Conflicts of Interest**

724 The authors declare no conflict of interest.

### 725 **References**

- 726 [1] Draper, S.; Adcock, T. A. A.; Borthwick, A. G. L.; Houlby, G. T. Estimate of the tidal stream  
727 power resource of the Pentland Firth. *Renew. Energy* **2014**, *63*, 650-657.
- 728
- 729 [2] Adcock, T. A. A.; Draper, S.; Houlby, G. T.; Borthwick, A. G.; Serhadlioglu, S. The available  
730 power from tidal stream turbines in the Pentland Firth. *Proc. R. Soc. A.: Math. Phys. Eng. Sci.*  
731 **2013**, *469* (2157), 1-21.
- 732
- 733 [3] Meygen LTD. MeyGen Tidal Energy Project Phase 1 Environmental Statement. Available  
734 online:  
735 [http://77.68.107.10/Renewables%20Licensing/MG\\_Sound\\_of\\_Stroma\\_Offshore\\_Tidal\\_Array/E](http://77.68.107.10/Renewables%20Licensing/MG_Sound_of_Stroma_Offshore_Tidal_Array/ES/Complete%20ES.pdf)  
736 [S/Complete%20ES.pdf](http://77.68.107.10/Renewables%20Licensing/MG_Sound_of_Stroma_Offshore_Tidal_Array/ES/Complete%20ES.pdf). (Accessed on 16 November 2015).
- 737
- 738 [4] Shields, M. A.; Dillon, L. J.; Woolf, D. K.; Ford, A.T. Strategic priorities for assessing  
739 ecological impacts of marine renewable energy devices in the Pentland Firth (Scotland, UK).  
740 *Marine Policy* **2011**, *33* (4), 635-642.
- 741
- 742 [5] Bonar, P.A.; Bryden, I.G.; Borthwick, A.G. Social and ecological impacts of marine energy  
743 development. *Renew. Sust. Energy Rev.* **2015**, *47*, 486-495.
- 744
- 745 [6] Neill, S.P.; Litt, E.J.; Couch, S.J.; Davies, A.G. The impact of tidal stream turbines on large-  
746 scale sediment dynamics. *Renew. Energy* **2009**, *34* (12), 2803-2812.
- 747
- 748 [7] Neill, S.P.; Jordan, J.R.; Couch, S.J. Impact of tidal energy converter (TEC) arrays on the  
749 dynamics of headland sand banks. *Renew. Energy* **2012**, *37* (1), 387-397.
- 750
- 751 [8] Martin-Short, R.; Hill, J.; Kramer; S. C.; Avdis, A.; Allison, P. A.; Piggott, M. D. Tidal resource  
752 extraction in the Pentland Firth, UK: Potential impacts on flow regime and sediment transport in  
753 the Inner Sound of Stroma. *Renew. Energy* **2015**, *76*, 596-607.
- 754
- 755 [9] Fairley, I.; Masters, I.; Karunarathna, H. The cumulative impact of tidal stream turbine arrays on  
756 sediment transport in the Pentland Firth. *Renew. Energy* **2015**, *80*, 755-769.
- 757
- 758 [10] Harendza, A. Benthic habitats in a tide-swept channel of the Pentland Firth and their potential  
759 responses to a tidal energy development. *Unpublished PhD thesis, University of Aberdeen,*  
760 *Aberdeen, UK, 2014.*
- 761
- 762 [11] Farrow, G. E.; Allen, N. H.; Akapan, E. B. Bioclastic carbonate sedimentation on a high-latitude,  
763 tide-dominated shelf. NE Orkney Islands, Scotland. *J. Sed. Petrol.* **1984**, *54* (2), 373-393.

764

- 765 [12] Kenyon, N.H.; Cooper, W.S. Sand banks, sand transport and offshore wind farms. *DTI Strategic*  
 766 *Environmental Assessment Area 6, Irish Sea, seabed and surficial geology and processes. British*  
 767 *Geological Survey. 2004.* Report CR/05/057. Available online:  
 768 [https://www.gov.uk/government/uploads/system/uploads/attachment\\_data/file/197293/SEA6\\_Geolog](https://www.gov.uk/government/uploads/system/uploads/attachment_data/file/197293/SEA6_Geology_BGS.pdf)  
 769 [y\\_BGS.pdf](https://www.gov.uk/government/uploads/system/uploads/attachment_data/file/197293/SEA6_Geology_BGS.pdf)  
 770
- 771 [13] Light, J. M.; Wilson, J. B. Cool-water carbonate deposition on the West Shetland shelf: a modern  
 772 distally steepened ramp. In *Carbonate ramps; Wright, V. P., Burchette, T. P., Eds.*; Geological  
 773 Society Special publications, **1998**, Volume 149, pp. 73-105.  
 774
- 775 [14] Holmes, R.; Bulat, J.; Henni, P.; Holt, J.; James, C.; Kenyon, N.; Leslie, A.; Long, D.; Musson,  
 776 R.; Pearson, S.; Stewart, H. DTI Strategic Environmental Assessment Area 5 (SEA5): Seabed  
 777 and superficial geology and processes. *British Geological Survey Report. 2005, CR/04/064N*  
 778
- 779 [15] Easton, M. C.; Woolf, D. K.; Bowyer, P. A. The dynamics of an energetic tidal channel, the  
 780 Pentland Firth, Scotland. *Cont. Shelf Res. 2013*, 48, 50-60.  
 781
- 782 [16] Goddijn-Murphy, L.; Woolf, D. K.; Easton, M. C. Current Patterns in the Inner Sound (Pentland  
 783 Firth) from Underway ADCP Data. *J. Atmos. Oceanic Technol. 2013*, 30, 96–111.  
 784
- 785 [17] Tamsett, D.; McIlvenny, J.; Watts, A. Colour sonar: multi-frequency sidescan sonar images of the  
 786 seabed in the Inner Sound of the Pentland Firth, Scotland. *J. Mar. Sci. Eng. 2016*, 4 (26), 1-18.  
 787
- 788 [18] Ramsdell, R. C.; Miedema, S. A.; Talmon, A. M. Hydraulic transport of sand/shell mixtures.  
 789 *Proceedings of the ASME 2011 30th International Conference on Ocean, Offshore and Arctic*  
 790 *Engineering OMAE2011 June 19-24. 2011*, Rotterdam, The Netherlands.  
 791
- 792 [19] Paphitis, D.; Collins, M. B.; Nash, A. I.; Wallbridge, S. Settling velocities and entrainment  
 793 thresholds of biogenic sands (shell fragments) under unidirectional flow. *Sedimentology 2002*,  
 794 49, 211–225.  
 795
- 796 [20] Flemming, B. W.; Schubert, H.; Hertweck, G.; Muller, K. Bioclastic tidal channel lag deposits: a  
 797 genetic model. *Senckenbergiana marit. 1992*, 22 (36), 109-129.  
 798
- 799 [21] Ashley, G.M. Classification of large-scale subaqueous bedforms: a new look at an old problem:  
 800 *J. Sed. Petrol. 1990*, 60, 160-172.  
 801
- 802 [22] Folk, R.L.; Ward, W.C. Brazos River bar: a study in the significance of grain size parameters. *J.*  
 803 *Sed. Petrol. 1957*, 27, 3–26.  
 804
- 805 [23] Tamsett, D.; Hogarth, P. Sidescan sonar beam function and seabed backscatter functions from  
 806 trace amplitude and vehicle roll data. *IEEE J. Oceanic Eng. 2015*, 41(1), 155-163.  
 807
- 808 [24] Pawlowicz, R.; Beardsley, B.; Lentz, S. Classical tidal harmonic analysis including error  
 809 estimates in MATLAB using T\_TIDE. *Computers & Geosciences. 2002*, 28, 929-937.

810

811 [25] Walters, R.A.; Casulli, V. A robust, finite element model for hydrostatic surface water flows.  
812 *Comm. Num. Methods Eng.* **1998**, 14, 931–940.

813

814 [26] Walters, R. A. Coastal ocean models: two useful finite element methods. *Cont. Shelf Res.* **2005a**,  
815 25(7), 775-793.

816

817 [27] Walters, R. A. A semi-implicit finite element model for non-hydrostatic (dispersive) surface  
818 waves. *Int. J. Num. Meth. Fluids* **2005b**, 49(7), 721-737.

819

820 [28] Gillibrand, P.A.; Lane, E.M.; Walters, R.A.; Gorman, R.M. Forecasting extreme sea surface  
821 height and coastal inundation from tides, surge and wave setup. *Austr. J. Civil Eng.* **2011**, 9, 99-  
822 112.

823

824 [29] Lane, E.M.; Gillibrand, P.A.; Arnold, J.R.; Walters, R.A. Tsunami inundation modeling with  
825 RiCOM. *Austr. J. Civil Eng.* **2011**, 9, 83-98.

826

827 [30] Walters, R.A.; Gillibrand, P.A.; Bell, R.; Lane, E.M. A Study of Tides and Currents in Cook  
828 Strait, New Zealand. *Ocean Dyn.* **2010**, 60, 1559-1580.

829

830 [31] Plew, D. R.; Stevens, C. L. Numerical modelling of the effect of turbines on currents in a tidal  
831 channel–Tory Channel, New Zealand. *Renew. Energy* **2013**, 57, 269-282.

832

833 [32] Walters, R. A.; Tarbotton, M. R.; Hiles, C. E. Estimation of tidal power potential. *Renew.*  
834 *Energy* **2013**, 51, 255-262.

835

836 [33] Egbert, G.D.; Erofeeva, S.Y. Efficient inverse modelling of barotropic ocean tides. *J. Atmos.*  
837 *Oceanic Technol.* **2002**, 19, 183–204.

838

839 [34] Dyke, P. P. G. *Coastal and Shelf Sea Modelling*, Springer US, New York, USA, 2001.

840

841 [35] Ferguson, R. I.; Church, M. A simple universal equation for grain settling velocity. *J. Sediment.*  
842 *Res.* **2004**, 74: 933–937.

843

844 [36] Durafour, M.; Jarano, A.; Le Bot, S.; Blanpain, O; Lafite, R.; Marin, F. In-situ study of the  
845 influence of size and shape of sediments on bedload transport. *Proceedings of the 7<sup>th</sup>*  
846 *International Conference on Coastal Dynamics, Bordeaux, France.* **2011**.

847

848 [37] Weill, P.; Mouazé, D.; Tessier, B.; Brun-Cottan, J. Hydrodynamic behaviour of coarse bioclastic  
849 sand from shelly cheniers, *Earth Surface Processes and Landforms* **2010**, 35 (14), 1642-1654.

850

851 [38] Shields, A. *Anwendung der Aehnlichkeitsmechanik und der Turbulenzforschung auf die*  
852 *Geschiebebewegung [Application of similarity mechanics and turbulence research on shear*  
853 *flow]. Mitteilungen der Preußischen Versuchsanstalt für Wasserbau* **1936**, 26, 5-24

854

- 855 [39] Valyrakis, M.; Diplas, P.; Dancy, C. L. Entrainment of coarse grains in turbulent flows: An  
856 extreme value theory approach, *Water Resources Res.* **2011**, 47(9), 1-17.  
857
- 858 [40] Smith, D.A.; Cheung, K.F. Transport rate of calcareous sand in unidirectional  
859 flow, *Sedimentology* **2005**, 52(5), 1009-1020.